Postprint of: Zielińska M., Rucka M., Detection of debonding in reinforced concrete beams using ultrasonic transmission tomography and hybrid ray tracing technique, CONSTRUCTION AND BUILDING MATERIALS, Vol. 262, (2020), 120104, DOI: 10.1016/j.conbuildmat.2020.120104

Detection of debonding in reinforced concrete beams using ultrasonic transmission tomography and hybrid ray tracing technique

Monika Zielińska[1]*, Magdalena Rucka[2]

[1] Department of Technical Fundamentals of Architectural Design, Faculty of Architecture, Gdańsk University of Technology, Narutowicza 11/12, 80-233 Gdańsk, Poland, email: monika.zielinska@pg.edu.pl

[2] Department of Mechanics of Materials and Structures, Faculty of Civil and Environmental Engineering, Gdańsk University of Technology, Narutowicza 11/12, 80-233 Gdańsk, Poland, email: magdalena.rucka@pg.edu.pl

* corresponding author

Abstract

This paper concerns inspection of reinforced concrete elements, with particular emphasis on assessing the quality of the adhesive connection between steel and concrete. A novel theoretical model was developed to determine the paths of transmitted, refracted and reflected elastic waves as well as a creeping wave propagated along the inclusion surface. Imaging the internal structure of tested beams was based on wave propagation measurements carried out on their surface and computed tomography. The ray tracing was performed by the hybrid approach as a combination of the network theory and the ray bending methods. The obtained results indicated a great potential of ultrasonic tomography in detection of debonding in reinforced concrete structures.

Keywords

reinforced concrete; debonding; damage imaging; ultrasonic tomography; ray tracing

1. Introduction

The condition assessment of reinforced concrete structures belongs to the greatest challenges of modern non-destructive testing. One of the most developed diagnostic techniques dedicated to damage detection in objects made of concrete are those utilizing the phenomenon of elastic wave propagation, including acoustic emission, ultrasound testing, impact echo or ultrasonic-pulse velocity methods (e.g. [1–5]). Previous studies have also shown high efficiency in the use of ultrasonic waves for detection of debonding between steel bars and concrete or defects of rebars; however, in most of conducted works measurements of ultrasonic waves were conducted on reinforcing bars (e.g. [6–9]). Recent research trends are moving towards imaging the internal structure of a tested element based on measurements carried out on its surface. Among various non-destructive methods, ultrasound transmission tomography is of great importance in providing valuable information about the interior of the material. The existing literature shows that this technique can be effectively used to visualise internal defects, anomalies and inclusions embedded in concrete structures or to verify the effectiveness of structural repairs. Schuller and Atkinson [10] demonstrated the possibility of detecting different types of internal voids in concrete by the acoustic tomography. They considered anomaly regions with high velocity (steel), zero velocity (void) and intermediate velocity (low-density concrete). Martin et al. [11] studied post-tensioned concrete beams, identifying both the location of ducts and voiding in ducts. Shiotani et al. [12] applied tomographic reconstruction of the velocity distribution of P-waves for quantitative assessment of repair work based on cement and epoxy injection. Aggelis et al. [13] applied tomography procedure based on numerical wave propagation signals to detect different types of inhomogeneities in concrete, such as voids, deteriorated zones and reinforcing bars. Choi and Popovics [14] proposed a through-thickness ultrasonic technique based on tomographic reconstruction represent internal defects in large concrete elements. Choi et al. [15] developed integrated ultrasound tomography and a three-dimensional computer vision technique. They obtained volumetric internal images to evaluate a full-scale reinforced concrete column. The elastic wave tomography was used by Chai et al. [16] to visualise the tendon duct filling, as well as honeycomb defects, in concrete elements. Haach and Ramirez [17] dealt with the use of the ultrasonic tomography to image the location of cylindrical polystyrene blocks in concrete prismatic samples. Lluveras Núñez et al. [18] tested the ultrasound tomography to detect bars/tubes of steel, PVC and aluminium embedded in cylindrical concrete specimens. Lu et al. [19] investigated the ultrasonic tomography for grouting quality evaluation. They

examined fourteen cube specimens to study how different parameters (such velocity difference between concrete and grout, the material of the pipe and the type of a pre-stressed tendon within the pipe) influenced tomograms. They also proposed a simplified theoretical model of a cross section with rebar; however, the model included only two paths, through the grouted pipe and around the pipe before grouting. Zielińska and Rucka [20] presented a condition assessment of masonry pillars using ultrasonic waves and computed tomography. The research focused on the characterization of the internal structure of the pillars containing internal inclusions in the form of a hole, a steel bar grouted by gypsum mortar, and a steel bar grouted by cement mortar.

The current challenge in ultrasound tomography is to assess the actual wave path from transmitter to receiver. Knowledge of the ray path is necessary to implement a weight matrix, which is part of the tomography algorithm. When a tested object is uniform or it contains regions characterized by moderate heterogeneity, the wave scattering effect is low, which make it possible to establish a straight wave transition. However, when the degree of material heterogeneity increases and material contains regions of significantly with higher or lower density, the refraction or reflection of the wave will occur inside the material, at boundaries between areas of different wave propagation velocities. In such case, the ray paths may bend around the inclusion of low velocity [10]. Previous studies showed that the assumption that the wave propagates in a straight line from the transmitter to the receiver can give satisfactory results (cf. [11–20]). However, a more appropriate approach is to take into account, the actual ray path. Early attempts at numerical ray tracing in ultrasound computerized tomography fields were presented by Andersen and Kak [21], and Bold and Birdsall [22]. Denis at al. [23] improved velocity image reconstruction by taking refraction into account. They compared straight and curved-ray approaches on the example of an agar-gel phantom. The problem of determination of the shortest path from a transmitter to the receiver was also described in Refs. [24–29]. Yanli [24] proposed algebraic reconstruction technique based on the shortest path ray tracing. The experiments conducted on concrete specimens with a circular void revealed that the use of shortest path ray tracing ensured more accurate imaging of the internal structures of concrete comparing with straight-line ray tracing. Ray-tracing algorithms, namely Dijkstra and A^* algorithms, were developed by Nowers et al. [25] and then applied them for inspecting an anisotropic weld. Lin et al. [26] studied a Dijkstra's path-finding algorithm as a ray tracing method to predict actual ultrasonic paths through multidirectional CFRP laminates. Espinosa et al. [27] used a ray-tracing method to evaluate the wood anisotropy and internal defects in oak disks tested. They concluded that curved rays should be

used to increase the quality of tomographic images. The network theory was investigated by Perlin and Pinto [28] to improve the ultrasonic tomography in concrete. Experiments were performed on concrete cubic specimens with internal inclusions of expanded polypropylene blocks. The results revealed the importance of ray tracing technique to improve tomograms. The most recently Perkowski and Tatara [29] presented a study on the imaging of brittle damage in concrete supported by the graph theory and Dijkstra's algorithm. They determined real paths of ultrasonic waves propagated in reinforced concrete samples subjected to three-point bending.

The main contribution of the paper is coupled theoretical-numerical-experimental research on the condition assessment of reinforced concrete beams. The inspection was conducted using ultrasonic waves and transmission computed tomography. The first part of the study was devoted to comprehensive investigations of elastic wave propagation in a beam cross section. A novel theoretical model was developed to determine the paths of transmitted, refracted and reflected elastic waves propagating through the cross section with an embedded circular inclusion as well as a creeping wave propagated along the inclusion surface. This model allowed the validation of the hybrid network theory/ray bending method used in ultrasonic computed tomography. The second part of the paper presents experimental investigations conducted to evaluate the possibility of using the ultrasonic tomography to assess the adhesive connection and to detect debonding between steel bar and concrete. The tomography imaging obtained for straight and curved ray paths was compared.

2. Elastic wave propagation in cross section with circular inclusion

The investigations conducted in this paper are focused on the ultrasonic wave propagation in a concrete cross section with a single inclusion of circular shape (Figure 1). The wave excited at a point on the external edge of the cross section propagates into the material with a circular wavefront. When the wave encounters a medium with different material parameters, it can be reflected or transmitted (and refracted). The intensity of reflection and transmission depends on the acoustic impedance of two adjacent media. The match of acoustic impedance of two media minimizes the reflection. On the other side, when the acoustic impedance of two adjacent media differs considerably, nearly total reflection occurs.

As the wave propagates through the boundary between different media, the relationship between the angles of incidence and refraction is governed by Snell's law. Knowing the wave

propagation velocities in both adjacent media (c_1 and c_2), for a specific angle of incidence α, it is possible to determine the refraction angle β according to the formula [30]:

$$\frac{\sin\alpha}{\sin\beta}=\frac{c_1}{c_2}. \tag{1}$$

2.1. Theoretical model

In this paper, we propose an accurate and complex theoretical model, enabling the determination of ray paths of ultrasonic waves propagating through a cross section with an embedded circular inclusion. Knowing the following parameters: the geometry of the cross section $(x_{\min}, x_{\max}, y_{\min}, y_{\max})$, the propagation velocities of the longitudinal wave in the medium surrounding the inclusion c_1 and in the inclusion itself c_2, the coordinates of the inclusion centre $I(x_I, y_I)$ and the inclusion radius r, one can determine the coordinates of the point $R(x_R, y_R)$ the wave will reach according to Snell's law. The location of this point is correlated with the position of the transmitter $T(x_T, y_T)$ and the angle φ at which the wave passes through the element (Figure 1b).

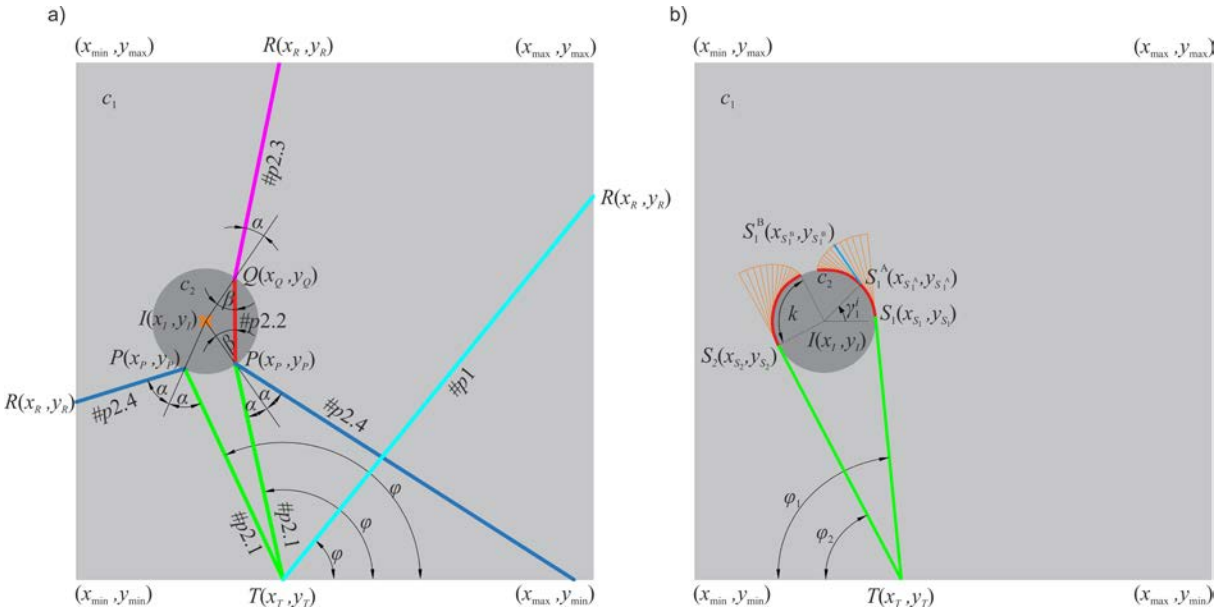

Figure 1. Scheme of wave propagation paths in the proposed theoretical model: a) transmitted, reflected and refracted paths, b) creeping wave reradiated along the tangent direction of the inclusion surface

The procedure for determining the point $R(x_R, y_R)$ to which the wave path comes from a specific point $T(x_T, y_T)$ and at a certain angle φ is presented below. The straight line traced from the transmitter location (x_T, y_T) at the angle φ can be described by the following equation:

$$Ax + By + C = 0\,, \tag{2}$$

Coefficients *A, B* and *C* take values, depending on the angle φ, as:

$$\begin{cases} A = -\tan\varphi,\ B = 1,\ C = -y_T + x_T \tan\varphi & \text{for } \varphi \neq 90^\circ \\ A = 1,\ B = 0,\ C = -x_T & \text{for } \varphi = 90^\circ \end{cases}. \tag{3}$$

The perpendicular distance of the inclusion centre to the straight line along which the wave passes through the element determines further direction of the wave. The distance *d* can be described by the formula:

$$d = \operatorname{sgn}(A)\frac{Ax_I + By_I + C}{\sqrt{A^2 + B^2}}. \tag{4}$$

If this distance is greater than or equal to the inclusion radius, i.e. $|d| \geq r$, ray path bypasses the inclusion and travels along a straight line to the edge of the element (path #p1 in Figure 1). The coordinates of point *R* can be determined from equations:

$$y_R = \begin{cases} \min(y_{\max}; \tan\varphi \cdot (x_{\max} - x_T)) & \text{for } \varphi \leq 90^\circ \\ \min(y_{\max}; \tan(180 - \varphi) \cdot x_T) & \text{for } \varphi > 90^\circ \end{cases}, \tag{5}$$

$$x_R = \frac{y_R}{\tan\varphi} + x_T\,. \tag{6}$$

In other cases, i.e. $|d| < r$, the wave encounters the inclusion, where it is reflected and refracted. This ray is denoted as path #p2 in Figure 1. The wave which reaches the border of two materials (path #p2.1) at point $P(x_P, y_P)$, goes to the adjacent medium, where is refracted at an angle β (path #p2.2). Then it returns to the medium surrounding the inclusion, refracting again at point $Q(x_Q, y_Q)$ at an angle α (path #p2.3). A remaining part of the wave energy is reflected (path #p2.4). For large values of the angle of incidence, i.e. $-1 > \sin\alpha \cdot (c_2 / c_1) > 1$, the wave can be completely reflected, without going to the adjacent medium. It should be noted, that the presented procedure takes into account only the first reflection from the inclusion.

Below the equations describing coordinates of the point of incidence for particular paths from #p2.1 to #p2.4 are given. The coordinates of point $P(x_P, y_P)$ for path #p2.1 can be determined from:

$$x_P = x_T + \cos\varphi \left(r\sin(90-\alpha)\frac{\tan\alpha}{\tan\left(\arcsin\left(\frac{d}{\sqrt{\left(x_T - x_I\right)^2 + \left(y_T - y_I\right)^2}}\right)\right)} - r\sin(90-\alpha) \right), \tag{7}$$

$$y_P = y_T + \sin\varphi \left(r\sin(90-\alpha)\frac{\tan\alpha}{\tan\left(\arcsin\left(\frac{d}{\sqrt{\left(x_T - x_I\right)^2 + \left(y_T - y_I\right)^2}}\right)\right)} - r\sin(90-\alpha) \right), \tag{8}$$

where the angle of incidence is:

$$\alpha = \arcsin\left(\frac{d}{r}\right). \tag{9}$$

The coordinates of point $Q(x_Q, y_Q)$ for path #p2.2 are given by:

$$x_Q = \cos(180+2\beta)(x_P - x_I) - \sin(180+2\beta)(y_P - y_I) + x_I, \tag{10}$$

$$y_Q = \sin(180+2\beta)(x_P - x_I) + \cos(180+2\beta)(y_P - y_I) + y_I, \tag{11}$$

where the refraction angle is

$$\beta = \arcsin\left(\sin\alpha\frac{c_2}{c_1}\right). \tag{12}$$

Path #p2.3 encounters the edge of the element at point *R* of coordinates:

$$x_R = x_Q + \operatorname{sgn}(x_{QR} - x_Q) d_a^{\,x}, \tag{13}$$

$$y_R = \frac{\left(x_R - x_Q\right)\left(y_{QR} - y_Q\right)}{\left(x_{QR} - x_Q\right)} + y_Q, \tag{14}$$

where:

$$x_{QR} = \cos(-180+\beta-\alpha)(x_P - x_Q) - \sin(-180+\beta-\alpha)(y_P - y_Q) + x_Q, \tag{15}$$

$$y_{QR} = \sin(-180+\beta-\alpha)(x_P - x_Q) + \cos(-180+\beta-\alpha)(y_P - y_Q) + y_Q, \tag{16}$$

$$x_a = \left[x_{\min} \quad x_{\max} \quad \frac{\left(y_{\min} - y_Q\right)\left(x_{QR} - x_Q\right)}{\left(y_{QR} - y_Q\right)} + x_Q \quad \frac{\left(y_{\max} - y_Q\right)\left(x_{QR} - x_Q\right)}{\left(y_{QR} - y_Q\right)} + x_Q \right], \tag{17}$$

$$d_a^{\,x} = \min\left(\left\{ \operatorname{sgn}(x_{QR} - x_Q) \cdot \left(x_a - x_Q\right) \right\}^+ \right). \tag{18}$$

The coordinates of point R for path #p2.4 are described by the formulas:

$$x_R = x_P + \operatorname{sgn}(x_{PR} - x_P) d_a^{\,x}, \tag{19}$$

$$y_R = \frac{(x_R - x_P)(y_{PR} - y_P)}{(x_{PR} - x_P)} + y_P, \tag{20}$$

where

$$x_{PR} = \cos(-2\alpha)(x_T - x_P) - \sin(-2\alpha)(y_T - y_P) + x_P, \tag{21}$$

$$y_{PR} = \sin(-2\alpha)(x_T - x_P) + \cos(-2\alpha)(y_T - y_P) + y_P, \tag{22}$$

$$x_a = \left[x_{\min} \quad x_{\max} \quad \frac{(y_{\min} - y_P)(x_{PR} - x_P)}{(y_{PR} - y_P)} + x_P \quad \frac{(y_{\max} - y_P)(x_{PR} - x_P)}{(y_{PR} - y_P)} + x_P \right], \tag{23}$$

$$d_a{}^x = \min\left(\left\{ \operatorname{sgn}(x_{PR} - x_P)(x_a - x_P) \right\}^+ \right). \tag{24}$$

Longitudinal wave that encounters the internal inclusion can not only be reflected and refracted, but also be partially converted into a creeping wave, which propagates on the inclusion surface (Figure 1b). This phenomenon is particularly important in the case of inclusions where the wave velocity is lower in relation to the surrounding medium, because this type of wave reaches the receiver on the opposite side faster than the wave passing through the inclusion. The length of the creeping wave path k depends on the time step t according to the formula:

$$k = c_1 t_2, \tag{25}$$

where

$$t_2 = t - \frac{\sqrt{(x_{S1} - x_T)^2 + (y_{S1} - y_T)^2}}{c_1}. \tag{26}$$

The path length k is measured from points S_1 and S_2 of coordinates:

$$x_{S1} = x_T + \operatorname{sgn}(\varphi_1)\cos(\varphi_1)\sqrt{(x_T - x_I)^2 + (y_T - y_I)^2 - r^2}, \tag{27}$$

$$y_{S1} = y_T + \operatorname{sgn}(\varphi_1)\sin(\varphi_1)\sqrt{(x_T - x_I)^2 + (y_T - y_I)^2 - r^2}, \tag{28}$$

$$x_{S2} = x_T + \operatorname{sgn}(\varphi_2)\cos(\varphi_2)\sqrt{(x_T - x_I)^2 + (y_T - y_I)^2 - r^2}, \tag{29}$$

$$y_{S2} = y_T + \operatorname{sgn}(\varphi_2)\sin(\varphi_2)\sqrt{(x_T - x_I)^2 + (y_T - y_I)^2 - r^2}, \tag{30}$$

where:

$$\varphi_1 = \arctan\left(\frac{y_T - y_I}{x_T - x_I}\right) - \arcsin\left(\frac{r}{\sqrt{(x_T - x_I)^2 + (y_T - y_I)^2}}\right), \tag{31}$$

$$\varphi_2 = \arctan\left(\frac{y_T - y_I}{x_T - x_I}\right) + \arcsin\left(\frac{r}{\sqrt{(x_T - x_I)^2 + (y_T - y_I)^2}}\right). \tag{32}$$

For each point $S_1^A(x_{S1}^A, y_{S1}^A)$ and $S_2^A(x_{S2}^A, y_{S2}^A)$ of the creeping wave path, the leaking energy reradiates along the tangent direction of the inclusion surface and converts into longitudinal waves, which wavefront is created by points $S_1^B(x_{S1}^B, y_{S1}^B)$ and $S_2^B(x_{S2}^B, y_{S2}^B)$:

$$x_{S1}^A(\gamma_1^i) = x_I + r\cos(\gamma_1^i), \tag{33}$$

$$y_{S1}^A(\gamma_1^i) = y_I + r\sin(\gamma_1^i), \tag{34}$$

$$x_{S2}^A(\gamma_2^i) = x_I + r\cos(\gamma_2^i), \tag{35}$$

$$y_{S2}^A(\gamma_2^i) = y_I + r\sin(\gamma_2^i), \tag{36}$$

$$x_{S1}^B(\gamma_1^i) = -\left(k - (r\gamma_1^i - (\varphi_1 - \mathrm{sgn}(\varphi_1)90)\frac{\pi}{180}\right)\sin(\gamma_1^i) + x_{S1}^A(\gamma_1^i), \tag{37}$$

$$y_{S1}^B(\gamma_1^i) = \left(k - (r\gamma_1^i - (\varphi_1 - \mathrm{sgn}(\varphi_1)90)\frac{\pi}{180}\right)\cos(\gamma_1^i) + y_{S1}^A(\gamma_1^i), \tag{38}$$

$$x_{S2}^B(\gamma_2^i) = -\left(k + (r\gamma_2^i - (\varphi_2 - \mathrm{sgn}(\varphi_2)90)\frac{\pi}{180}\right)\sin(\gamma_2^i) + x_{S2}^A(\gamma_2^i), \tag{39}$$

$$y_{S2}^B(\gamma_2^i) = \left(k + (r\gamma_2^i - (\varphi_2 - \mathrm{sgn}(\varphi_2)90)\frac{\pi}{180}\right)\cos(\gamma_2^i) + y_{S2}^A(\gamma_2^i), \tag{40}$$

where:

$$\gamma_1^i \in \left\langle (\varphi_1 - \mathrm{sgn}(\varphi_1)90)\frac{\pi}{180}; (\varphi_1 - \mathrm{sgn}(\varphi_1)90)\frac{\pi}{180} + \frac{k}{r} \right\rangle, \tag{41}$$

$$\gamma_2^i \in \left\langle (\varphi_2 - \mathrm{sgn}(\varphi_2)90)\frac{\pi}{180} - \frac{k}{r}; (\varphi_2 - \mathrm{sgn}(\varphi_2)90)\frac{\pi}{180} \right\rangle. \tag{42}$$

Below is an example illustrating the ray paths determined by the proposed model. Simulations were carried out for a concrete section with dimensions of 10 × 10 cm^2, containing a circular inclusion with a diameter of 2 cm located at point $I(2.5\text{ cm}, 5\text{ cm})$. The position of transmitter *T* was constant and equal $x_T = 0.5$ cm, $y_T = 0$ cm. Figure 2 presents all possible ray paths determined using the above-described procedure. Only the first reflection from the inclusion was considered. Rays paths were calculated for the angle φ changing between 0° and 180° with a step of 2° at selected time instances, in both the section with steel bar and the section with air void. The connection of points marked by the ray paths for a specific time steps, allowed to determine the wavefronts. The process of finding the wavefront was shown for four selected time instances, namely 14 μs, 15.5 μs and 22 μs. Considering the section with the steel bar (Figure 2a), it can be seen that the wavefront in the vicinity of the steel bar propagates faster that the wavefront in concrete. In the case of the section with the

air void (Figure 2b), the wavefront has a delay due to the large difference in wave propagation velocity in concrete and air.

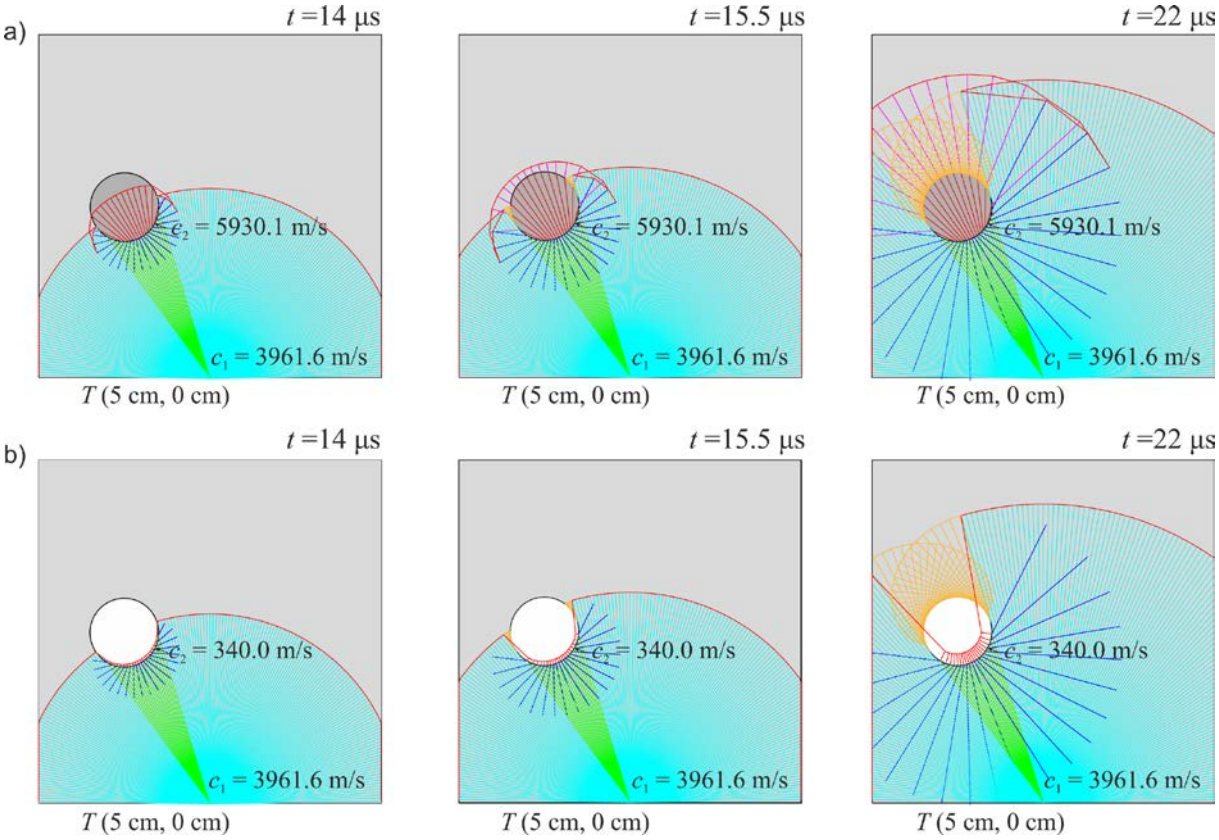

Figure 2. Paths of waves traced using the proposed model in concrete element with inclusion at selected time instances: a) steel inclusion; b) circular air void

In order to verify the wavefront traced using the proposed theoretical model, finite element method (FEM) simulations of the stress wave propagation were carried out in the Abaqus/Explicit software (cf. [20]). The simulation result is given in Figure 3 in the form of a snapshot of the magnitude of the displacement field at the selected time instances equal to 14 μs, 15.5 μs, and 22 μs for both types of inclusions, namely steel bar (Figure 3a) and circular void (Figure 3b). High compatibility of numerical and theoretical wavefronts allowed confirming the correctness of the proposed theoretical model.

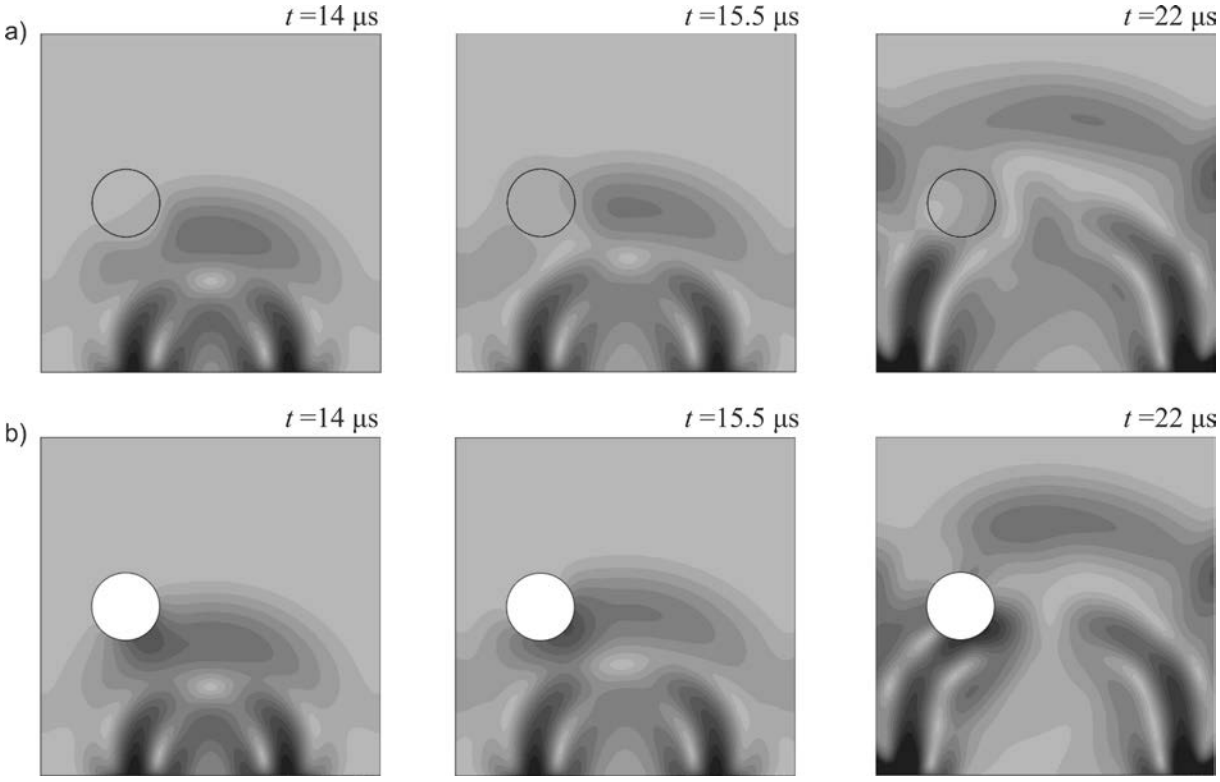

Figure 3. FEM snapshots of wave propagation patterns in concrete element with inclusion at selected time instances: a) steel inclusion; b) circular air void

2.2. Dijkstra's algorithm for ray tracing

Diagnostics using ultrasonic waves is mainly based on the travel time from the transmitter to the receiver. This involves the need to specify a path with the shortest wave transition time. The propagation path between the transmitter and receiver is governed by Fermat's principle. The principle states that the actual path between two given points is that which minimize the transition time between them. This path can be determined based on Snell's law, according to Eq. (1). However, such an approach may be not possible in the case of elements with unknown internal geometry. The solution may be using the ray-tracing technique based on the network theory, which was developed by Moser [31,32] for calculation of the shortest paths of seismic waves. In the network theory method, the region of interest is first discretized by a grid of interconnected points, and next efficient path-finding algorithms are used to determine globally minimal travel time [25,26,28,29,33].

In this paper, Dijkstra's algorithm [34] was used to determine the fastest wave path in a concrete section with areas of variable speed of ultrasonic wave propagation. The algorithm takes into account a table of nodes between which the wave path can travel. The solution is based on the velocity of wave propagation between two adjacent nodes and the distance between them. All nodes are divided into two groups. In the first group (group I) there are

nodes for which the transit time is known. The second group (group II) contains the remaining elements. The schema od Dijkstra's method includes the following steps (e.g. [25,28,29]):

1. Assign all nodes to group II and give them an infinite cost except start node, which cost is zero.
2. Choose node from group II with the lowest value. Name it as *S* (start node) and transfer this node to group I.
3. Name as *N* (neighbour node) each node from group II that is connected to node *S*.
4. Calculate time travel between *S* and each *N* node using equation:

$$t(S) = \min(t(S); t(N) + t_{SN}), \tag{43}$$

$$t_{SN} = \frac{d_{SN}}{\frac{(v_S + v_N)}{2}}, \tag{44}$$

   where t(S) denotes the travel time to reach node *S*, $t(N)$ denotes the travel time to reach node *N*, t_{NS} is the travel time between nodes *S* and *N*, d_{NS} is the distance between nodes *S* and *N*, v_S and v_N are the values of the ultrasonic wave velocity in nodes *S* and *N*, respectively.
5. Repeat steps 2-4 until group II is empty.

Dijkstra's algorithm assumes checking each node. This ensures that a global, optimal solution is obtained for the entire tested model.

Examples presented below illustrate the procedure of determination of the shortest paths and times using Dijkstra's algorithm. Analyses were performed for a concrete cross section of dimensions 10 × 10 cm^2 with an inclusion in the form of steel bar with a diameter of 2 cm. In the first stage, the fastest ray path was determined using Snell's law (Figure 4). The positions of the transmitter (*T*) and the receiver (*R*) were predefined. The ray passed through three sections; however, two of them had the same material parameters. Therefore, it was possible to determine the angle of incidence α equal to 11.47° and the angle of refraction β equal to 17.33° (Figure 4a). Using these angles, it was possible to calculate transition time for each section and the total transition time as 24.53 μs (Figure 4b).

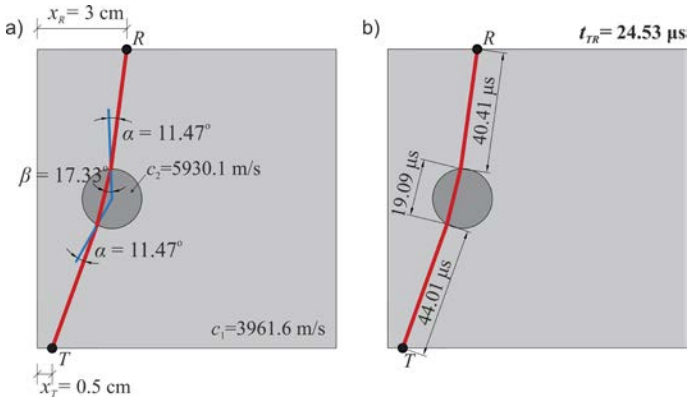

Figure 4. Determination of the fastest path between transmitter (*T*) and receiver (*R*) in concrete cross section containing circular inclusion: a) wave path determined using Snell's law; b) path lengths in sub-areas and total transition time t_{TR}

The same calculation example was solved using Dijkstra's algorithm. It was assumed that the wave could travel between nodes located on the element edges and on the border between the steel bar and concrete section, as shown in Figure 5. On both bottom and top edges of the concrete section, 19 nodes were assumed. The border between concrete and steel was divided by 36 nodes into sections about 17 mm long. Using such discretization, ray-tracing was simulated from transmitter T (x_T = 0.5 cm) to receiver R (x_R = 3 cm). Figure 6 illustrates selected results of searching for the fastest wave path between nodes *T* and *R*. Nine different paths are presented and total transition time for each of them is given. The fastest wave path was found for the case depicted in the first diagram in Figure 6. The result obtained was compared with the path determined using Snell's law (Figure 4b). Transition time for individual sections differed slightly due to the discretization used (Figure 5); however, in both cases the same total time of transition (24.53 µs) was obtained.

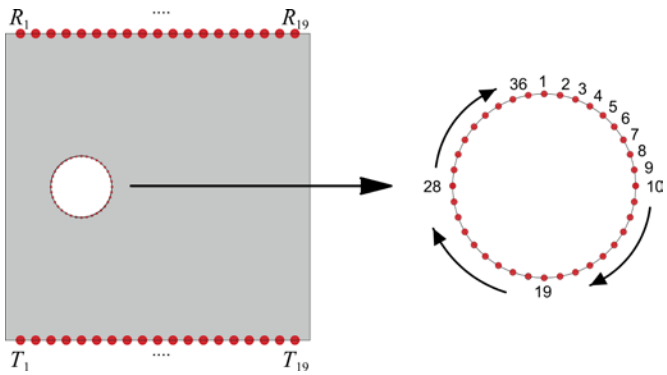

Figure 5. Arrangement of transmitting (*T*) and receiving (*R*) points and location of nodes on the border between concrete and steel inclusion.

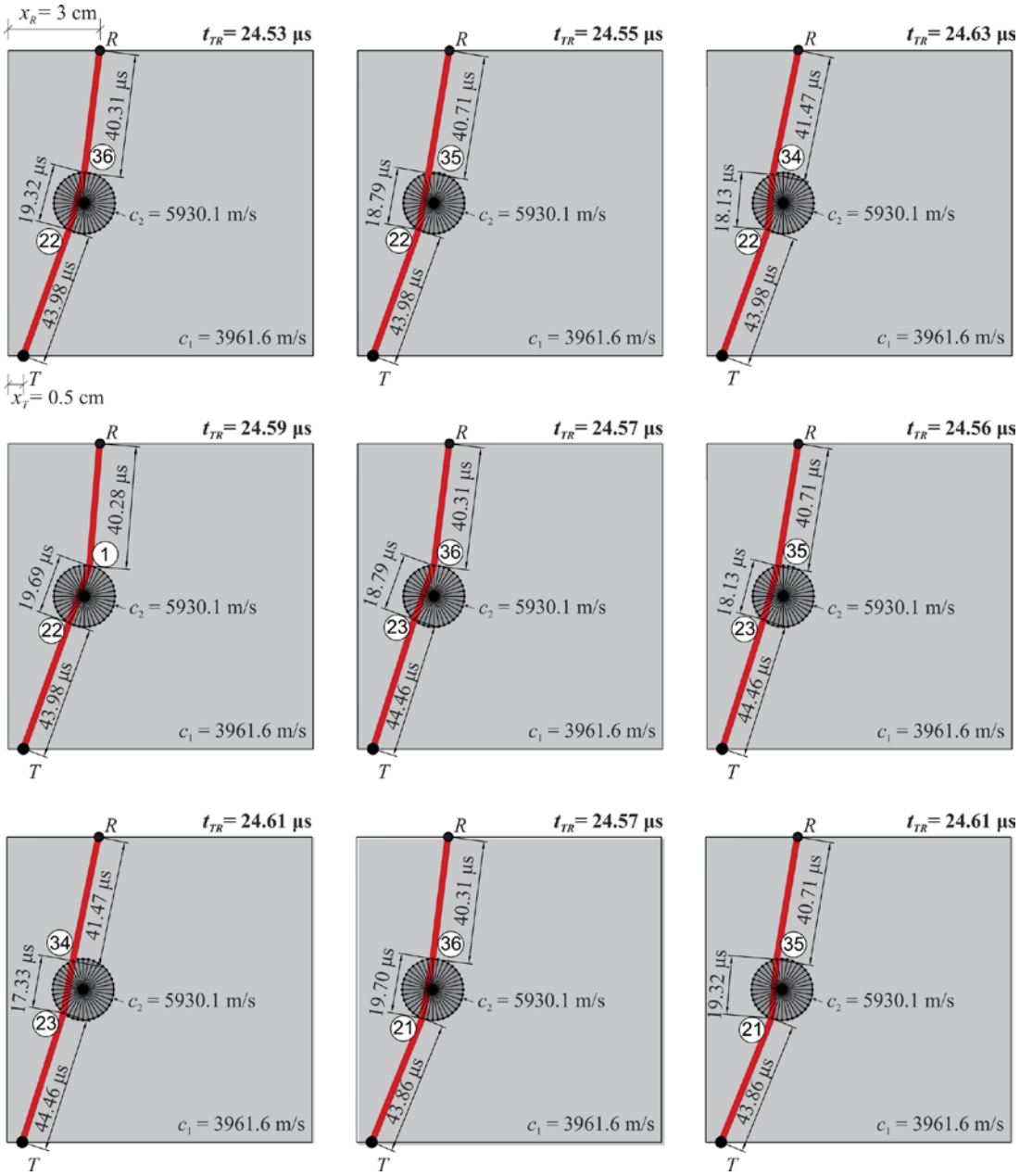

Figure 6. Selected results of searching for the fastest wave path from transmitter (*T*) to receiver (*R*) using Dijkstra algorithm

Finally, the effect of the inclusion material was analysed. The inclusion was simulated by modifying the wave velocity with the coefficient ω, which was defined as the ratio of the longitudinal wave in concrete (c_1) to the longitudinal wave velocity in the circular inclusion (c_2):

$$\omega = \frac{c_2}{c_1}. \tag{45}$$

In the example, the velocity of longitudinal wave propagation in concrete was assumed as 3961 6 m/s, while in the inclusion area the velocity was simulated as a higher (for $\omega > 1$) and lower ($\omega < 1$) than for concrete. The following variants of the ω parameter were used:

– $\omega = 1.15 \rightarrow c_2 = 4555.8$ m/s,
– $\omega = 1.10 \rightarrow c_2 = 4357.8$ m/s,
– $\omega = 1.05 \rightarrow c_2 = 4159.7$ m/s,
– $\omega = 0.95 \rightarrow c_2 = 3763.5$ m/s,
– $\omega = 0.90 \rightarrow c_2 = 3565.4$ m/s,
– $\omega = 0.85 \rightarrow c_2 = 3367.4$ m/s.

Results of calculating the wave paths using Dijkstra's algorithm are shown in Figure 7. The paths from transmitters (T_1 to T_{19}) to receivers (R_1 to R_{19}) were calculated. A clear deflection of paths can be observed already for the parameters ω = 1.10 and 0.9. For inclusions with a propagation velocity greater than the surrounding material ($\omega > 1$), the rays focus in the inclusion area. In the case when the parameter ω is less than one ($\omega < 1$), the rays bypass the inclusion. Figure 8 additionally shows the paths for inclusions made in the form of a hole (ω = 0.09), and steel bar (ω = 1.50). Note that the model presented above is idealized, and the points where the path may bend are located only on the media border.

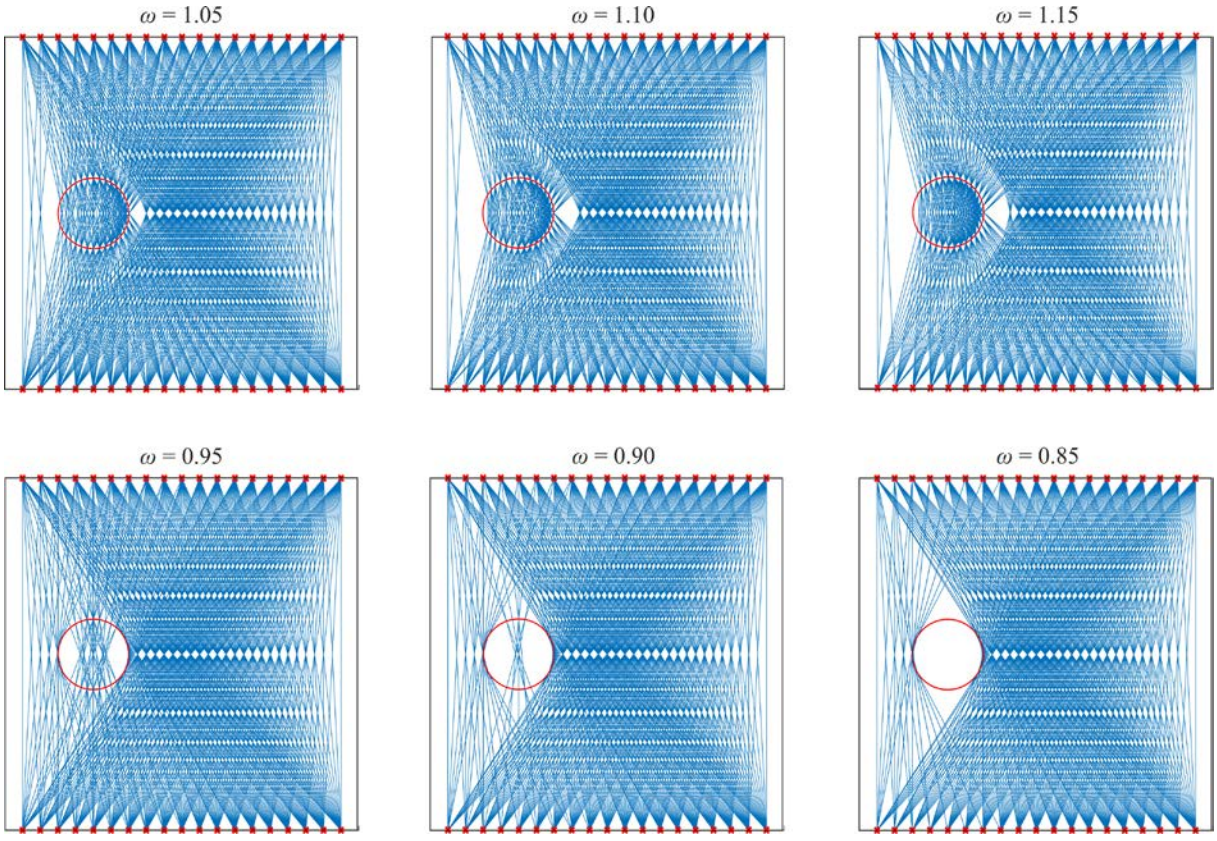

Figure 7. Ray tracing results using Dijkstra's algorithm for concrete section with inclusion of different values of parameter ω

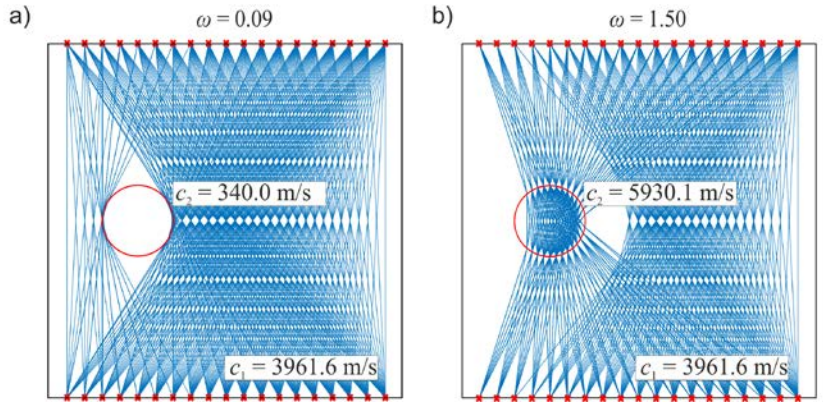

Figure 8. Ray tracing results using Dijkstra's algorithm for concrete section with inclusion: a) steel inclusion; b) circular air void

3. Ultrasonic computed tomography

Ultrasonic transmission tomography allows reconstructing the internal structure of a tested element based on information obtained from wave propagation signals passing through it. A scheme of cross sectional reconstruction is illustrated in Figure 9. The procedure begins with the division of the section into cells also known as pixels. They are marked with dashed lines in Figure 9a. Then, signals of ultrasonic waves passing through the tested specimen from the transmitter (*T*) to the receivers (*R*) are collected (Figure 9a, b). The result of ultrasonic transmission tomography is the velocity distribution within the medium. To each pixel, a specific, constant value of the wave propagation velocity is assigned (Figure 9c).

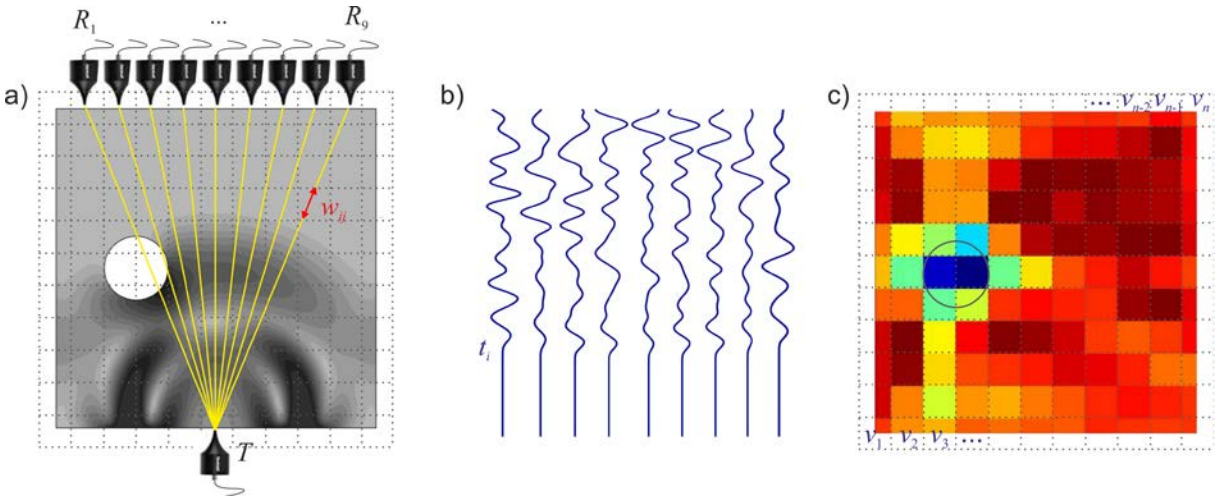

Figure 9. Schematic diagram of ultrasonic transmission tomography: a) cross section divided into pixels, with indicated transmitter, receivers and simulated wave field; b) wave propagation signals; c) tomographic reconstruction image

A typical information used in the image reconstruction is the time-of-flight (TOF). It can be represented by a line integral of the transition time distribution along the propagation way *w*:

$$t = \int_T^R dt = \int_T^R s dw = \int_T^R \frac{1}{v} dw, \tag{46}$$

where v is the average velocity, and s is the inverse of the velocity referred as the slowness. Based on the known element geometry and the TOF from the transmitter to the receiver, it is possible to determine the average velocity of wave propagation. The reconstitution of the velocity profile for each pixel (1,2,3,...,n), based on the time-of-flight obtained from ray paths (1,2,3,...,m), can be performed using the following formula:

$$t_i = \sum_{j=1}^{n} w_{ij} \frac{1}{v_j} = \sum_{j=1}^{n} w_{ij} s_j, \quad i = 1,2,3,\ldots,m, \quad j = 1,2,3,\ldots,n, \tag{47}$$

where w_{ij} denotes the transition way of the i-ray through the j-pixel, t_i denotes the transition time of the P-wave between the transmitter and receiver along the i-ray, v_j is the velocity at pixel j and s_j is the slowness at pixel j.

The system of linear equations given by Eq. (47), can be expressed in a matrix form with known transition time along a given path (matrix **t**) and the length of the path passing through the cell (matrix **w**), and with unknown slowness (matrix **s**):

$$\mathbf{t}_{m\times 1} = \mathbf{w}_{m\times n}\mathbf{s}_{n\times 1}. \tag{48}$$

In the transmission tomography, the above system of equations usually has more equations than unknowns which means that it is an overdetermined problem. Therefore, special methods of solution have to be used. One of the most effective approach to solve such problems are iterative methods which include the algebraic reconstruction technique (ART) [35]. The ART involves calculating the time-of-flight for an assumed velocity in each pixel, comparing the calculated TOFs with measured ones and iterative modification of the velocity until a convergence criterion is achieved. In the first stage, each cell adopts the same value of the wave propagation velocity (i.e. the average velocity of wave propagation) assuming an examined section is homogeneous. Elastic waves in this case propagate along straight lines (Figure 10, 1st column). Then the iteration process begins and the correction is calculated according to the equation [36]:

$$s_j^{(k)} = s_j^{(k-1)} + \frac{w_{ij}\Delta t_i}{\sum_{j=1}^{n} w_{ij}^2}. \tag{49}$$

where Δt_i is the difference between the time of the original projection and the rebuilding time. After the first iteration, the object is no longer treated as composed of regions with constant propagation velocity; therefore, the path of the wave transition does not have to travel from the transmitter to the receiver in a straight line.

In this paper, the ray tracing is performed by the so-called hybrid approach, which is a combination of the network theory and the ray bending methods (e.g. [37–39]). The new path is determined based on the value of the wave propagation velocity in individual pixels. The ray tracing follows Fermat's principle according to which the path of first arrival is the shortest. The network method is used that creates a network of connected nodes. The wave path can only move between these nodes. After building the node network, there are several combinations of wave transition from transmitter to receiver. To determine which path is the fastest, Dijkstra's algorithm is used. This method guarantees a global minimum time, but the traced paths are angular and seem unnatural (Figure 10, 2nd column). However, it can be a starting point for iterative improvement of their course through the ray bending algorithm. The straight lines are divided into an increasing number of straight, but not collinear segments. The paths produced in this way are more smoothly curved. At each iteration, the travel time is calculated. The process end when convergence is reached (Figure 10, 3rd column). Based on the newly determined paths the **w** matrix from Eq. (48) is redefined. The process of iterative determination of the pixel slowness by the ART method is performed again. The procedure is repeated until a convergence criterion is achieved.

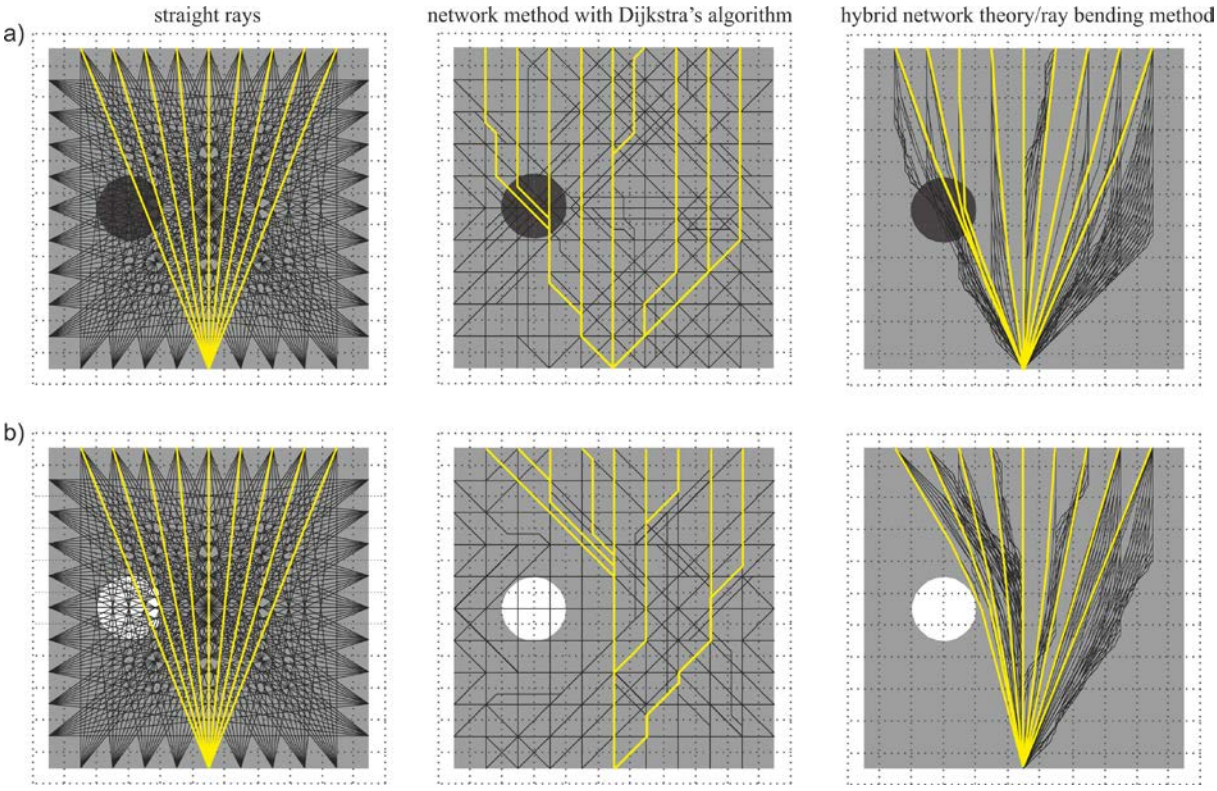

Figure 10. Schematic diagram of ray tracing approaches: straight rays (1st column), network method with Dijkstra algorithm (2nd column) and hybrid network theory/ray bending method (3rd column) on the example of concrete cross section containing circular inclusion: a) steel bar; b) circular air void

Paths of waves traced using the hybrid network theory/ray bending method were validated by the proposed theoretical model. The results for the concrete cross section

with steel bar and with air void are compared in the Figure 11. The paths from both methods show high convergence, which confirmed the correctness of using the hybrid method for ray tracing.

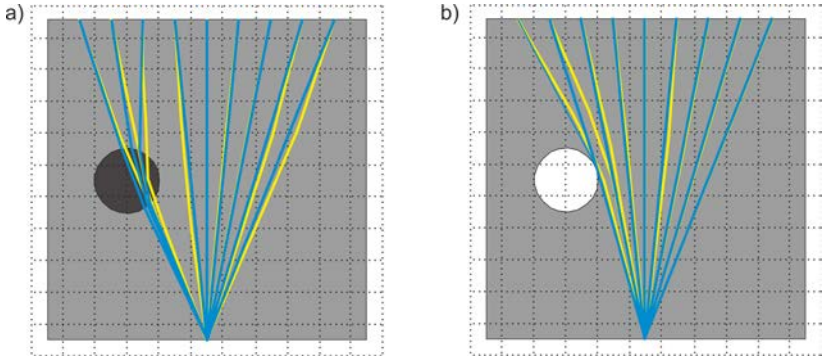

Figure 11. Comparison of the wave paths traced by the theoretical model (blue lines) and hybrid network theory/ray bending method (yellow lines) for concrete cross section containing circular inclusion: a) steel bar; b) circular air void

4. Experimental investigations of debonding imaging in reinforced concrete beams

4.1. Description of specimens

Ultrasonic investigations were performed on concrete beams with external dimensions of 10 cm x 10 cm x 50 cm (Figure 12a). The samples were made of concrete including the following ingredients: Portland cement type CEM I 42.5R (340 kg/m^3), sand 0–2 mm (755 kg/m^3), aggregate 2–8 mm (1130 kg/m^3) and water (180 kg/m^3).

Four concrete beams were tested in this study. The first beam (#1) was prepared as a reference model. It was a purely concrete object, with no inclusions. Beams #2, #3 and #4 had a circular inclusion with a diameter of 2 cm (Figure 12b), situated at a distance of x_I = 2.5 cm, y_I = 5 cm. Beam #2 contained an embedded steel bar. In beam #3, the bar was tightly wrapped three times with a cellophane film with a thickness of about 30 μm to obtain a defect in the form of a thin layer of debonding between steel and concrete. Previous studies revealed that introducing a cellophane film provides a decrease of adhesion at the interface between steel and concrete introducing a discontinuity of stresses and displacements of propagating waves while providing some indirect contact between steel and concrete and maintaining the ability to carry a certain value of load in a pull-out test (e.g. [40]). Beam #4 contained a hole that was formed with a PVC pipe with a wall thickness equal 1 mm. This beam was intended to simulate the state of complete separation of bar from the concrete. The photographs of tested samples are given in Figure 12c.

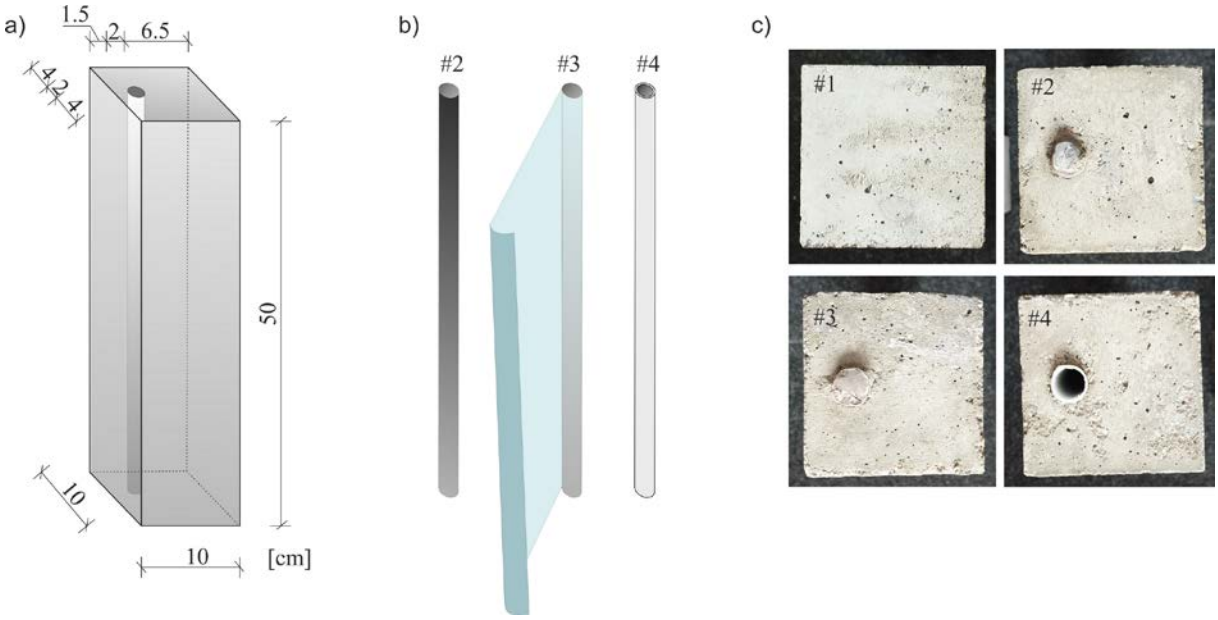

Figure 12. Geometry of tested beams: a) 3D view with dimensions; b) types of inserts used to form inclusions (steel bar, steel bar wrapped with cellophane film and PVC pipe); c) plane views of specimens #1 to #4

4.2. Equipment, data acquisition and processing

Experiments were conducted using the ultrasonic pulse velocity (UPV) method. The experimental setup is shown in Figure 13. The PUNDIT PL-200 was applied for measurements the time-of-flight (TOF) of the P-wave between two 54 kHz exponential transducers. The transducers were used in the through transmission mode, and dry coupling was applied between them and the tested structure.

Ultrasonic measurements were carried out in the cross section in the middle of the beam height. Measurement points were distributed at each beam edge (9 points at each edge, with a distance of 1 cm). The configuration of the measurement points is illustrated in Figure 14. The receiving transducer (*R*) was set at a given point, and then the transmitting transducer (*T*) was moved from the first to the last point on the opposite wall. From each transmitting point, transition times along 9 paths were registered. In total, transition times were measured along 162 paths. The applied mesh consisted of 121 pixels, resulting in a 1 cm mesh.

To perform tomographic reconstruction, the authors' computer programs were developed in the Matlab® software. The image reconstruction algorithm was based on the ART method. The tomographic velocity maps were created using both straight ray paths and curved ray paths. To determine the curved paths, a grid of nodes was created in accordance with the network method. Each of 121 pixel was divided into nine equal squares. The nodes were in the center of each square resulting in 961 nodes. In order to find the fastest path Dijkstra's algorithm was implemented. Then the paths were bent according to the ray bending method.

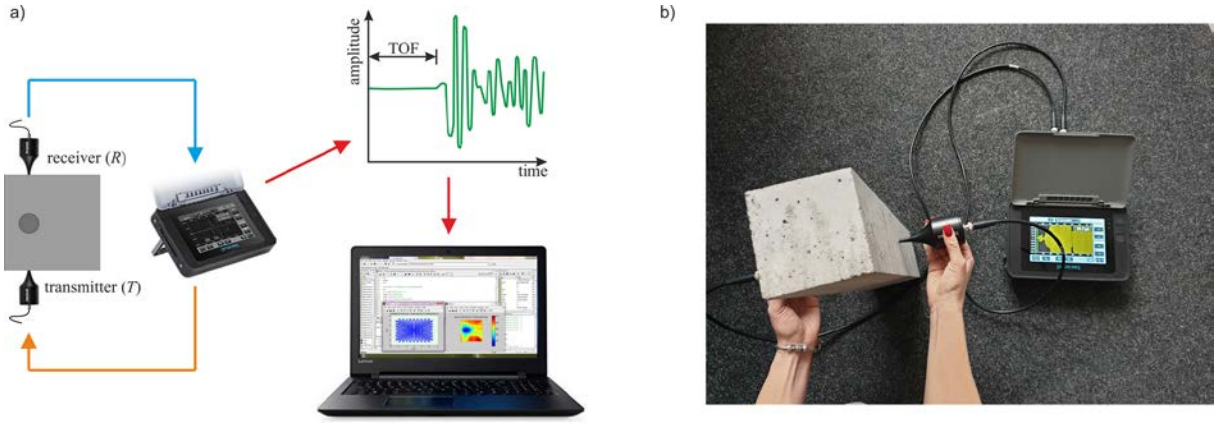

Figure 13. Experimental setup: a) schematic diagram of test rig; b) photograph of measurements in through transmission mode

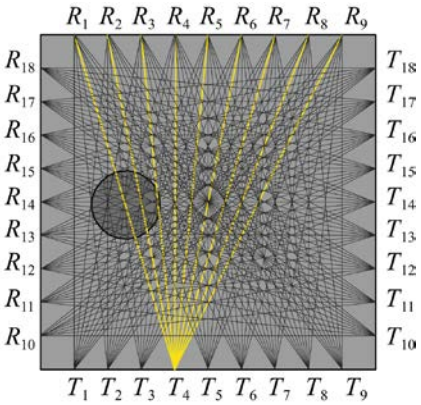

Figure 14. Configuration of measurement points and paths (transmission of waves at points T_1-T_{18} and sensing of waves at points R_1-R_{18})

4.3. Results

Ultrasound tomography images are shown in Figures 15, 16, 17 and 18 for tested beams #1, #2, #3 and #4, respectively. Velocity maps were calculated using both straight-line paths and curved rays determined by the hybrid network theory/ray bending method. In each set of results given in Figures 15 to 18, the first columns shows tomogram with indicated position of inclusion, the second – tomogram with rays and the third – traced rays. Each tomographic velocity image has its own colorbar with values covering the entire range of velocities.

The tomographic velocity maps for the intact beam (#1), did not show significant changes in the wave velocity on the tested cross section (Figure 15). The difference between the smallest and the largest velocities was about 180 m/s for straight-line paths and about 300 m/s for curved paths. There are visible two areas, namely the area with smaller values of velocity at a bottom part of the beam and the area in the central and top part of the beam with higher values of velocity. It may be result of concentration of course aggregate at the bottom of the beam, which has been confirmed by its visual inspection.

Measurements made on the specimen with the steel bar (#2) revealed a clear region with a higher value of wave propagation velocity (Figure 16). However, the shape of this region varied with the approach used for ray tracing. When the straight rays were used in the ultrasonic transmission tomography, the area was spread, while for curved rays it was more concentrated. The difference between the minimum and maximum velocities was about 450 m/s for straight paths and about 900 m/s for curved paths. These values were much higher compared to the intact beam. The traced curved rays were concentrated at the location of the steel bar, because of the increase of wave propagation velocity in this area. This indicated a good adhesive connection between the bar and the surrounding concrete.

Figure 17 shows the results for the beam with the cellophane wrapped steel bar (# 3). This kind of inclusion was intended to simulate the lack of adhesive connection between the bar and the concrete. The location of the inclusion is visible on the maps as an area with reduced wave propagation velocities, indicating debonding of the bar from concrete. The difference between velocities for maps with straight-line and curved paths was about 350 m/s and 700 m/s, respectively. The use of the straight rays resulted to obtain satisfactory results; however, the damage imaging was improved when the network theory combined with ray bending approach was applied. In such a case, the area identified was more concentrated and closer to the actual size. Analysing the traced rays it can be observed that if the paths were curved they bypassed the inclusion area.

The tomographic velocity maps (Figure 18) for the beam with a PVC pipe (# 4) revealed similar patterns as those for the beam with debonding (#3). It indicated that the ultrasonic tomography method was very sensitive in detection of defects in adhesive bonding, even in the case of debonding zone of very small thickness. Analysing the maps for the beam with air void, the location of the inclusion was also indicated as a region with reduced velocities. However, the map created based on curved paths showed greater uniformity on the area beyond the inclusion. The difference between the smallest and the largest velocities was about 400 m/s for straight-line paths and about 700 m/s for curved paths. The course of curved paths was similar to the beam # 3, i.e. the waves also bypassed the inclusion site.

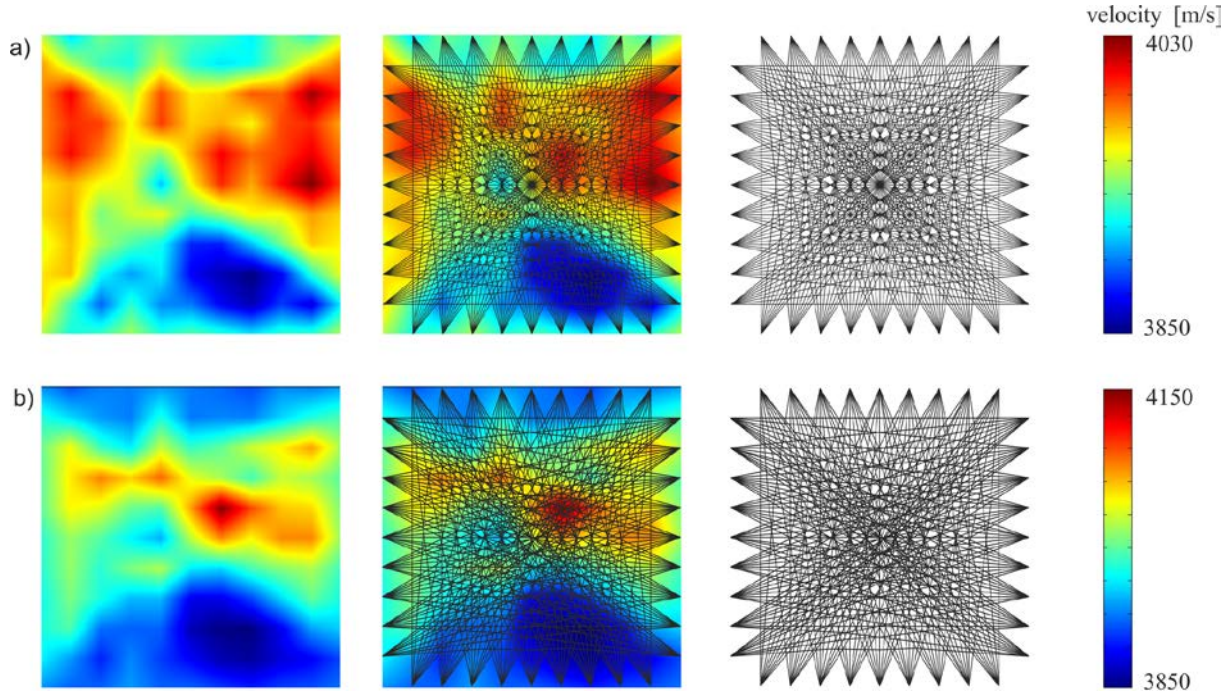

Figure 15. Tomographic velocity images for intact beam #1: a) straight-line paths, b) curved rays determined by hybrid network theory/ray bending technique

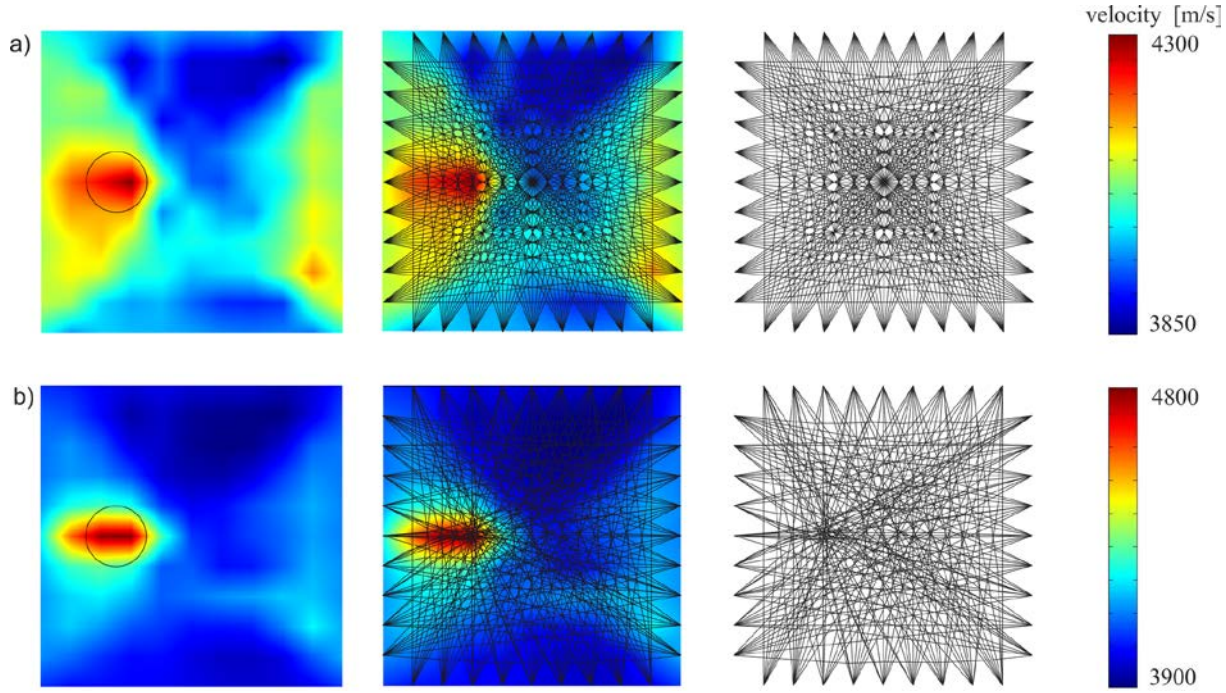

Figure 16. Tomographic velocity images for beam #2 with a steel bar: a) straight-line rays, b) curved rays determined by hybrid network theory/ray bending technique

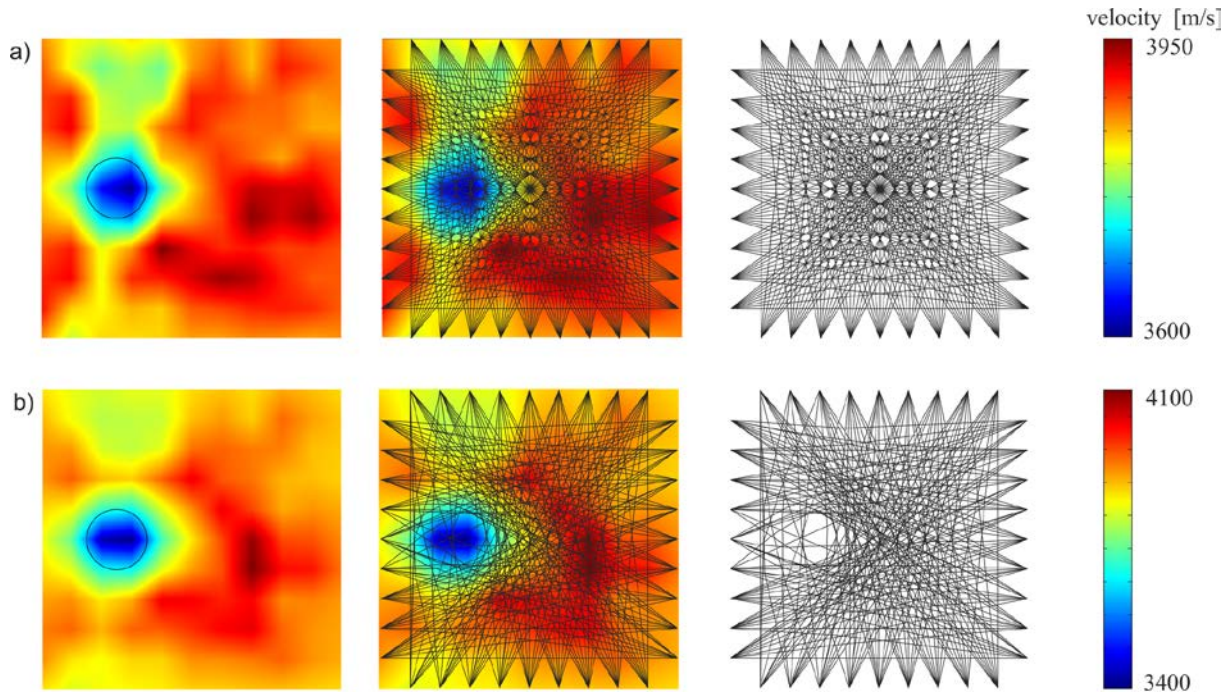

Figure 17. Tomographic velocity images for beam #3 with a cellophane wrapped steel bar: a) straight-line paths, b) curved rays determined by hybrid network theory/ray bending technique

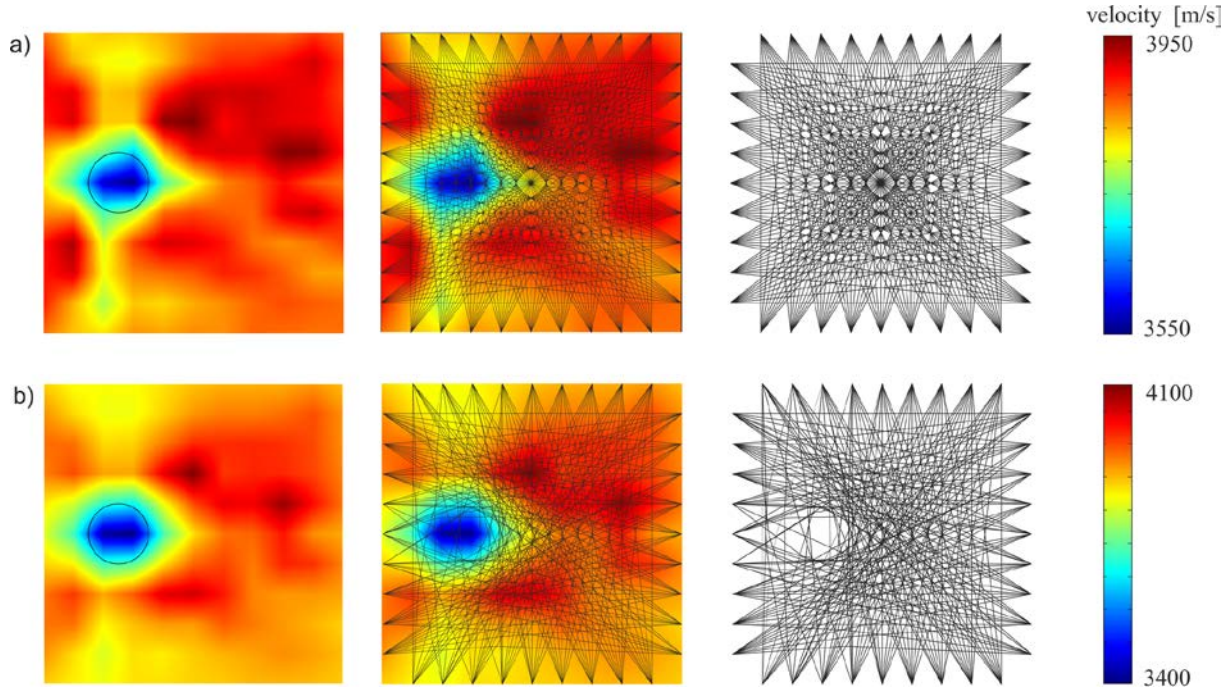

Figure 18. Tomographic velocity images for beam #4 with a PVC pipe: a) straight-line paths, b) curved rays determined by hybrid network theory/ray bending technique

Table 1 presents a quantitative analysis of the wave propagation velocity in each of the four considered beams. The minimum, maximum and average velocities for the intact element (#1) and elements with inclusions in the form of a steel bar (#2), a bar wrapped with cellophane (#3) and PVC pipe (#4) are listed. Additionally, the measures of variability, i.e. the standard deviation (SD) and coefficient of variation (CV), were calculated.

The highest average value of the wave propagation velocity of 4036.23 m/s was obtained for the specimen with the steel bar (beam #2). The specimens with a cellophane wrapped bar (beam #3) and a PVC pipe (beam #4) revealed similar average velocity values of 3865.32 m/s and 3879.49 m/s, respectively. The standard deviation and the coefficient of variation also reached the highest values for the model with the steel bar. In this case, the standard deviation was equal to 17.17 m/s, while the coefficient of variation 0.43%. The smallest values of both coefficients were for the intact beam, where the standard deviation was equal to 7.83 m/s, while the coefficient of variation 0.20%

Table 1. Wave propagation velocities in tested concrete beams (#1-#4).

Concrete beam	v_{min} [m/s]	v_{max} [m/s]	$\Delta v = v_{max} - v_{min}$ [m/s]	v_{avg} [m/s]	SD [m/s]	CV [%]
#1	3749.81	4166.67	416.86	3950.62	7.83	0.20
#2	3579.64	4502.67	923.03	4036.23	17.17	0.43
#3	3480.10	4110.36	630.25	3865.32	10.72	0.28
#4	3355.70	4064.28	708.57	3879.49	11.44	0.29

Conclusions

In this paper, the condition assessment of concrete beams was carried out by the ultrasonic transmission tomography. The experimental and theoretical studies were aimed at verification how different inclusions in concrete beam affected the propagation of ultrasonic waves.

The developed theoretical model was proved to enable precise determining ray paths of ultrasonic waves propagating through a cross section with an embedded circular inclusion. The fastest path, which is the most important in the transmission ultrasound tomography, was calculated using hybrid approach. It was found that using Dijkstra's algorithm resulted in paths with a global minimum time, but an angular and unnatural shape. The application of the network theory combined with ray bending approach enabled obtaining paths consistent with the theoretical model.

Conducted experimental investigations focused on the possibility of imaging different inclusions in a concrete cross section. Research was carried out on four laboratory specimens: one concrete beam and three concrete beams containing circular inclusions in the form of steel bar, debonded steel bar and air void. The cross sectional image was based on the reconstruction of the propagation velocity of ultrasonic waves. The steel bar was identified in tomograms as an area higher velocity values while the air void as an area with lower velocity values. It was found the use of the straight rays allowed to obtain satisfactory tomograms.

However, the application of the hybrid network theory/ray bending approach increased the quality of reconstruction, improving the imaging of the shape and size of the defect. The course of curved paths varied depending on the inclusion material. If the inclusion was characterized by a higher propagation velocity than the surrounding medium, then the rays accumulated in the inclusion area. For inclusions with lower velocity, the rays bypassed the place of inclusion. The quantitative analysis of the wave propagation values in the reconstructed images of beams containing an inclusion allowed concluding that the difference between the minimum and maximum velocities was about twice as larger for curved paths as compared to straight paths.

Conducted study have also confirmed the high efficiency of ultrasonic tomography in imaging of the lack of adhesion between reinforcing bar and concrete, despite very small thickness of introduced debonding (about 90 μm). The tomogram obtained for the bar wrapped with a cellophane film was similar to that for the air void, i.e. it contained a distinct area with lower values of wave propagation velocity. It indicated large sensitivity of ultrasonic waves excited and measured on the concrete element surface to the debonding-type defects.

Acknowledgments

The research work was carried out within the project No. 2017/27/N/ST8/02399, financed by the National Science Centre, Poland.

References

[1] K. Schabowicz, Ultrasonic tomography - The latest nondestructive technique for testing concrete members - Description, test methodology, application example, Arch. Civ. Mech. Eng. 14 (2014) 295–303. doi:10.1016/j.acme.2013.10.006.

[2] G. Karaiskos, A. Deraemaeker, D.G. Aggelis, D. Van Hemelrijck, Monitoring of concrete structures using the ultrasonic pulse velocity method, Smart Mater. Struct. 24 (2015) 113001. doi:10.1088/0964-1726/24/11/113001.

[3] M. Rucka, K. Wilde, Ultrasound monitoring for evaluation of damage in reinforced concrete, Bull. Polish Acad. Sci. Tech. Sci. 63 (2015) 65–75. doi:10.1515/bpasts-2015-0008.

[4] S. Beniwal, D. Ghosh, A. Ganguli, Ultrasonic imaging of concrete using scattered elastic wave modes, NDT E Int. 82 (2016) 26–35. doi:10.1016/j.ndteint.2016.04.003.

[5] A. Garbacz, T. Piotrowski, L. Courard, L. Kwaśniewski, On the evaluation of interface quality in concrete repair system by means of impact-echo signal analysis, Constr. Build. Mater. 134 (2017) 311–323. doi:10.1016/j.conbuildmat.2016.12.064.

[6] W.B. Na, T. Kundu, M.R. Ehsani, Lamb waves for detecting delamination between steel bars and concrete, Comput. Civ. Infrastruct. Eng. 18 (2003) 58–63.

doi:10.1111/1467-8667.t01-1-00299.

[7] F. Wu, F.-K. Chang, Debond detection using embeddded piezoelectric elements for reinforced concrete structures - Part II: Analysis and algorithm, Struct. Heal. Monit. 5 (2006) 17–28.

[8] Y. Lu, J. Li, L. Ye, D. Wang, Guided waves for damage detection in rebar-reinforced concrete beams, Constr. Build. Mater. 47 (2013) 370–378. doi:10.1016/j.conbuildmat.2013.05.016.

[9] B. Zima, R. Kędra, Reference-free determination of debonding length in reinforced concrete beams using guided wave propagation, Constr. Build. Mater. 207 (2019) 291–303. doi:10.1016/j.conbuildmat.2019.02.143.

[10] M.P. Schuller, R.H. Atkinson, Evaluation of concrete using acoustic tomography, in: Rev. Prog. Quant. Nondestruct. Eval., 1995: pp. 2215–2222.

[11] J. Martin, K.J. Broughton, A. Giannopolous, M.S.A. Hardy, M.C. Forde, Ultrasonic tomography of grouted duct post-tensioned reinforced concrete bridge beams, NDT E Int. 34 (2001) 107–113. doi:10.1016/S0963-8695(00)00035-9.

[12] T. Shiotani, S. Momoki, H. Chai, D.G. Aggelis, Elastic wave validation of large concrete structures repaired by means of cement grouting, Constr. Build. Mater. 23 (2009) 2647–2652. doi:10.1016/j.conbuildmat.2009.01.005.

[13] D.G. Aggelis, N. Tsimpris, H.K. Chai, T. Shiotani, Y. Kobayashi, Numerical simulation of elastic waves for visualization of defects, Constr. Build. Mater. 25 (2011) 1503–1512. doi:10.1016/j.conbuildmat.2010.08.008.

[14] H. Choi, J.S. Popovics, NDE application of ultrasonic tomography to a full-scale concrete structure, IEEE Trans. Ultrason. Ferroelectr. Freq. Control. 62 (2015) 1076–1085. doi:10.1109/TUFFC.2014.006962.

[15] H. Choi, Y. Ham, J.S. Popovics, Integrated visualization for reinforced concrete using ultrasonic tomography and image-based 3-D reconstruction, Constr. Build. Mater. 123 (2016) 384–393. doi:10.1016/j.conbuildmat.2016.07.010.

[16] H.K. Chai, K.F. Liu, A. Behnia, K. Yoshikazu, T. Shiotani, Development of a tomography technique for assessment of the material condition of concrete using optimized elastic wave parameters, Materials (Basel). 9 (2016) 291. doi:10.3390/ma9040291.

[17] V.G. Haach, F.C. Ramirez, Qualitative assessment of concrete by ultrasound tomography, Constr. Build. Mater. 119 (2016) 61–70. doi:10.1016/j.conbuildmat.2016.05.056.

[18] D. Lluveras Núñez, M.Á. Molero-Armenta, M.Á.G. Izquierdo, M.G. Hernández, J.J.A. Velayos, Ultrasound transmission tomography for detecting and measuring cylindrical objects embedded in concrete, Sensors (Switzerland). 17 (2017) 1085. doi:10.3390/s17051085.

[19] J. Lu, S. Tang, X. Dai, Z. Fang, Investigation into the Effectiveness of Ultrasonic Tomography for Grouting Quality Evaluation, KSCE J. Civ. Eng. 22 (2018) 5094–5101. doi:10.1007/s12205-018-0091-x.

[20] M. Zielińska, M. Rucka, Non-Destructive Assessment of Masonry Pillars using Ultrasonic Tomography, Materials (Basel). 11 (2018) 2543. doi:10.3390/ma11122543.

[21] A.C. Anderson, A.H. Kak, Digital ray tracing in two-dimensional refractive index fields, J. Acoust. Soc. Am. 72 (1982) 1593–1606.

[22] T.G. Bold, G.E.J. Birdsall, A top-down philosophy for accurate numerical ray tracing, J. Acoust. Soc. Am. 80 (1986) 656–660.

[23] F. Denis, O. Basset, G. Gimenez, Ultrasonic Transmission Tomography in Refracting Media: Reduction of Refraction Artifacts by Curved-Ray Techniques, IEEE Trans. Med. Imaging. 14 (1995) 173–188. doi:10.1109/42.370414.

[24] Y. Chu, The shortest path ray tracing algorithm in concrete computerized tomography, in: 2010 Int. Forum Inf. Technol. Appl., 2010: pp. 392–396. doi:10.1109/IFITA.2010.307.

[25] O. Nowers, D.J. Duxbury, J. Zhang, B.W. Drinkwater, Novel ray-tracing algorithms in NDE: Application of Dijkstra and A* algorithms to the inspection of an anisotropic weld, NDT E Int. 61 (2014) 58–66. doi:10.1016/j.ndteint.2013.08.002.

[26] L. Lin, H. Cao, Z. Luo, Dijkstra's algorithm-based ray tracing method for total focusing method imaging of CFRP laminates, Compos. Struct. 215 (2019) 298–304. doi:10.1016/j.compstruct.2019.02.086.

[27] L. Espinosa, F. Prieto, L. Brancheriau, P. Lasaygues, Effect of wood anisotropy in ultrasonic wave propagation: A ray-tracing approach, Ultrasonics. 91 (2019) 242–251. doi:10.1016/j.ultras.2018.07.015.

[28] L.P. Perlin, R.C. de A. Pinto, Use of network theory to improve the ultrasonic tomography in concrete, Ultrasonics. 96 (2019) 185–195. doi:10.1016/j.ultras.2019.01.007.

[29] Z. Perkowski, K. Tatara, The Use of Dijkstra's Algorithm in Assessing the Correctness of Imaging Brittle Damage in Concrete Beams by Means of Ultrasonic Transmission Tomography, Materials (Basel). 13 (2020) 551. doi:10.3390/ma13030551.

[30] J.L. Rose, Ultrasonic Guided Waves in Solid Media, Cambridge University Press, New York, 2014. doi:10.1017/CBO9781107273610.

[31] T.J. Moser, The shortest path method for seismic ray tracing in complicated media, Faculteit Aardwetenschappen der Rijksuniversiteit te Utrecht, 1992.

[32] T.J. Moser, Shortest path calculation of seismic rays, Geophysics. 56 (1991) 59–67. doi:10.1190/1.1442958.

[33] P. Qiu, R. Hu, L. Hu, Q. Liu, Y. Xing, H. Yang, J. Qi, T. Ptak, A numerical study on travel time based hydraulic tomography using the SIRT algorithm with Cimmino iteration, Water (Switzerland). 11 (2019). doi:10.3390/w11050909.

[34] E.W. Dijkstra, A note on two problems in connexion with graphs, Numer. Math. 1 (1959) 269–271. doi:10.1007/BF01386390.

[35] A.C. Kak, M. Slaney, Principles of Computerized Tomographic Imaging, The Instituite of Electrical and Electronics Engineers, Inc., New York, 1988.

[36] E.F. Oliveira, S.B. Melo, C.C. Dantas, D.A.A. Vasconcelos, L.F. Cadiz, Comparison among tomographic reconstruction algorithms with a limited data, in: Int. Nucl. Atl. Conf. - Ina., 2011.

[37] M.J. Jackson, D.R. Tweeton, 3DTOM: Three-Dimensional Geophysical Tomography, 1996.

[38] H.J.A. Van Avendonk, A.J. Harding, J.A. Orcutt, J.S. McClain, A two-dimensional tomographic study of the Clipperton transform fault, J. Geophys. Res. 103 (1998) 17885–17899. doi:10.1029/98jb00904.

[39] H.J.A. Van Avendonk, A.J. Harding, J.A. Orcutt, W. Steven Holbrook, Hybrid shortest path and ray bending method for traveltime and raypath calculations, Geophysics. 66 (2001) 648–653. doi:10.1190/1.1444955.

[40] B. Zima, M. Rucka, Guided ultrasonic waves for detection of debonding in bars partially embedded in grout, Constr. Build. Mater. 168 (2018) 124–142. doi:10.1016/j.conbuildmat.2018.02.107.